PCCP

PAPER

View Article Online
View Journal | View Issue

Check for updates

Cite this: *Phys. Chem. Chem. Phys.*, 2021, **23**, 26401

Bulk band structure of Sb_2Te_3 determined by angle-resolved photoemission spectroscopy

Henriette E. Lund,[a] Klara Volckaert,[a] Paulina Majchrzak,[a] Alfred J. H. Jones,[a] Marco Bianchi,[a] Martin Bremholm[a] and Philip Hofmann *[b]

Received 2nd September 2021,
Accepted 12th November 2021

DOI: 10.1039/d1cp04031f

rsc.li/pccp

The bulk band structure of the topological insulator Sb_2Te_3 is investigated by angle-resolved photoemission spectroscopy. Of particular interest is the dispersion of the uppermost valence band with respect to the topological surface state Dirac point. The valence band maximum has been calculated to be either near the Brillouin zone centre or in a low-symmetry position in the $\bar{\Gamma}$–$\bar{M}$ azimuthal direction. In order to observe the full energy range of the valence band, the strongly p-doped crystals are counter-doped by surface alkali adsorption. The data show that the absolute valence band maximum is likely to be found at the bulk Γ point and predictions of a low-symmetry position with an energy higher than the surface Dirac point can be ruled out.

Published on 12 November 2021. Downloaded on 1/20/2026 5:39:56 PM.

1 Introduction

Sb_2Te_3 was one of the first materials recognised as a three-dimensional topological insulator (TI) with a single Dirac cone surface state.[1,2] Its electronic structure is very similar to both that of Bi_2Se_3 and Bi_2Te_3, materials that are viewed as prototypical for this family of TIs.[3] An important point is that both Bi_2Se_3 and Bi_2Te_3 are plagued by degenerate n-doping due to common crystalline defects such that they are ill-suited for experimentally assessing or technologically exploiting transport through the surface states instead of the bulk states. Sb_2Te_3, on the other hand, is typically strongly p-doped due to the presence of substitutional Sb on Te sites.[4]

As a consequence of the p-doping, only the lower part of the surface state Dirac cone is accessible to angle-resolved photoemission spectroscopy (ARPES) experiments that are routinely used to characterise the predicted surface state dispersion of TIs[5] but can only access filled states. This problem can be circumvented by strong surface doping *via* the adsorption of alkali metals[6] or by pumping of electrons into unoccupied states.[7] The surface state dispersion can also be characterised by scanning tunnelling spectroscopy in the presence of a strong magnetic field, *via* the energy spacing of the resulting Landau levels.[8]

The existence of metallic surface states in TIs is enforced by a band inversion, *i.e.*, a swapping of the *p*/*d*-like valence band (VB) with the s-like conduction band around a high symmetry point, leading to a "negative" band gap. More precisely, the relation of the parity invariants $\delta(\Gamma_i)$ of the eight time-reversal invariant momenta in the bulk Brillouin zone[9] dictates the **k** position of the "negative" band gap and the Fermi contour topology of the surface states. For Sb_2Te_3 and most similar crystals, $\delta(\Gamma)$ is -1 while it is 1 for all the other time-reversal invariant momenta, implying a negative band gap at the bulk Γ point and that the surface $\bar{\Gamma}$ point is encircled by a single non spin-degenerate surface Fermi contour.

The negative band gap has a number of interesting consequences for the effect of many-body interactions on the overall electronic structure of the TIs. In a conventional (non-topological) semiconductor, many-body corrections as implemented in a GW calculation mostly serve to correct the well-known tendency of density functional theory (DFT) to underestimate the size of the band gap. This happens by an approximately rigid shift of VBs and conduction bands away from each other. In a TI, this rigid increase of the band gap still takes place in most of the Brillouin zone (BZ) but not in the region of the negative band gap.[12–16] This leads to a **k**-dependent deformation of the bands which may result in wrong predictions about the band structure and topology.[17] Sb_2Te_3 serves as an excellent example of this. DFT calculations along high-symmetry directions typically place the absolute VB maximum (VBM) between the Z and F points of the BZ,[11,18] see Fig. 1(a) and (b). The inclusion of many-body corrections such as realised in the GW approximation changes this picture and places the absolute VBM at the bulk Γ point.[10,15,16] Actually, merely displaying the band structure between Z and F may not even show the correct position of the VBM in the DFT calculations because the true VBM could be at any position in the plane given by the $\bar{\Gamma}$–$\bar{M}$ direction in the surface BZ[10] (blue shaded plane in Fig. 1(a)),

[a] *Department of Physics and Astronomy, Interdisciplinary Nanoscience Center (iNANO), Aarhus University, 8000 Aarhus C, Denmark*
[b] *Department of Chemistry, Interdisciplinary Nanoscience Center (iNANO), Aarhus University, 8000 Aarhus C, Denmark. E-mail: philip@phys.au.dk*

Published on 12 November 2021. Downloaded on 1/20/2026 5:39:56 PM.

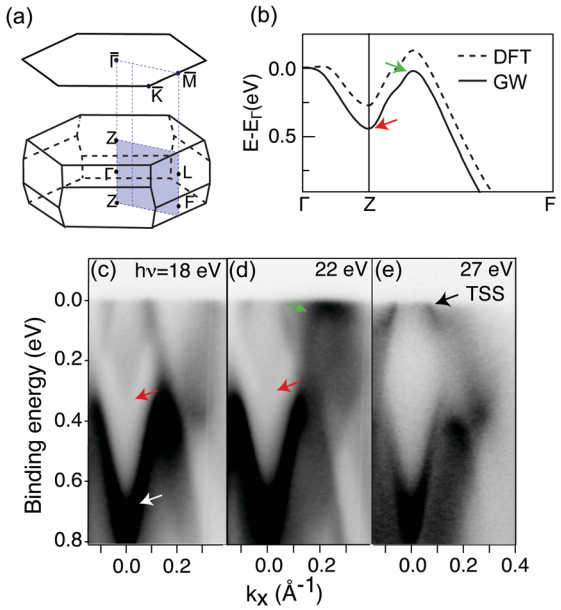

Fig. 1 (a) Bulk Brillouin zone of Sb_2Te_3 together with the projected surface Brillouin zone. The VB maximum is predicted to be placed either near Γ or in the shaded plane along the $\bar{\Gamma}$–$\bar{M}$ azimuthal direction. (b) Calculations of the bulk band structure using density functional theory with and without additional GW corrections from ref. 10 and 11, respectively. The calculations have been shifted so as to align at the band maximum at Γ, E_Γ, which is also chosen as the energy zero. (c)–(e) Photoemission intensity as a function of binding energy and k_x (in the direction along $\bar{\Gamma}$–$\bar{M}$), collected at photon energies of 18, 22 and 27 eV, respectively. Several features are marked: the bottom of the VB along Γ–Z (red arrow), the branch of the VB forming a local maximum in the shaded plane (green arrow), the topological surface state (TSS, black arrow) and a further deeper lying surface state (white arrow). The photoemission intensity is scaled such that dark corresponds to high intensity and the colour scale has been saturated to show the relevant features at the Fermi level.

so that the true VBM in DFT might be even higher than the one between Z and F. Note that the band structure differences between GW and DFT are not small and can exceed 100 meV, a quarter of the total width of the highest VB along Γ–Z. A similar interplay between absolute VBM position and many-body corrections takes place in Bi_2Se_3[19] and Bi_2Te_3.[20]

The question of where the absolute VBM is found is not only of interest as a benchmark for many-body corrections in band structure calculations, it also has important consequences for the TIs' transport properties. In particular, the relative position of surface state Dirac point and bulk state dispersion restricts the range of energies in which surface state-dominated transport is achievable.[21] In a DFT surface band structure calculation, the absolute VBM in the $\bar{\Gamma}$–$\bar{M}$ plane lies above the Dirac point of the topological surface state,[2,11] implying that no level of doping would result in a situation where electronic transport could be dominated by the surface state electrons near the Dirac point. On the other hand, such surface-dominated transport is possible when the VBM in the $\bar{\Gamma}$–$\bar{M}$ direction lies below the surface state Dirac point.

Synchrotron radiation-based ARPES studies were able to map the relevant bulk band structure for Bi_2Se_3[19] and Bi_2Te_3,[20] underlining the importance of the corrections in the GW calculations. However, the aforementioned p-doping makes the band structure determination of Sb_2Te_3 by ARPES more challenging because relevant states can be placed above the Fermi energy in a degenerately doped crystal. Several ARPES investigations from Sb_2Te_3 single crystal surfaces have been published,[2,6,7,22,23] as well as from thin films[24,25] where the doping can be better controlled by growth conditions.[26] The focus of most studies was the topological surface states. Here we study the dispersion of the topmost VB in order to determine the position and energy of the global VBM. We exploit variable photon energies to explore the complete $\bar{\Gamma}$–$\bar{M}$ plane. We gain access to the normally unoccupied states by doping the surface with alkali atoms. A similar approach has been used in ref. 6 in order to access the surface state Dirac point by ARPES.

2 Experimental details

Sb_2Te_3 crystals were grown following the procedure outlined in ref. 27. Attempts were made to synthesize bulk crystals with a smaller p-doping or to achieve chemical bulk counter-doping but these were not successful. ARPES experiments were performed on the SGM-3 beamline of ASTRID2 in Aarhus.[28] Samples were cleaved at room temperature in a pressure better than 5×10^{-7} mbar, prior to the measurement at 2×10^{-10} mbar. The sample temperature during ARPES measurements was $\approx$35 K. Energy and angular resolution were better than 50 meV and 0.1°, respectively. Rb was dosed from a well-outgassed SAES Getters dispenser during the acquisition of photoemission data. As expected, Rb adsorption leads to a strong electrostatic doping effect but the adsorption on the Sb_2Te_3 surface is highly unstable. Stopping the Rb evaporation leads to an immediate loss of doping. The Rb coverage was estimated using core level spectroscopy. However, due to the unstable adsorption, this cannot be measured at the same time as the VB spectra but requires a separate cleave of the sample and the evaporation of Rb under the same conditions.

3 Results and discussion

We start out by presenting data from as-cleaved samples. Due to the p-doping of the material, the VBM at Γ and the surface state Dirac point are above the Fermi energy E_F and thus not accessible to ARPES. However, inspecting data from pristine surfaces – instead of alkali-doped samples – has the advantage of giving higher quality spectra and the data is thus useful for identifying the salient features and their approximate position in three-dimensional k-space.

Photoemission spectra taken along the $\bar{\Gamma}$–$\bar{M}$ azimuthal direction (defined as k_x) for different photon energies are shown in Fig. 1(c)–(e). The highest intensity feature in Fig. 1(c)–(e) is a surface state in a projected bulk band gap of the VB (marked by a white arrow). This state and its Rashba-splitting have been studied in detail in ref. 22 and 23. A second surface

 This journal is © the Owner Societies 2021

Published on 12 November 2021. Downloaded on 1/20/2026 5:39:56 PM.

state is the metallic topological surface state forming a Dirac cone around the $\bar{\Gamma}$ point (marked as TSS). Due to the p-doping, only the lower part of the Dirac cone is visible, most clearly in Fig. 1(e).

The bulk features of interest are the highest VB at $\bar{\Gamma}$ and a possible further VBM in the $\bar{\Gamma}$–$\bar{M}$ plane. Starting with the former, a GW calculation of the highest VB gives an absolute energy difference of only ≈450 meV between the Γ and Z point of the BZ[10] with the highest binding energy reached at the Z point (see Fig. 1(b)). This total bandwidth can be small compared to the energy broadening due to the short inelastic mean free path of the photoelectrons and the resulting uncertainty in k_z, so that the entire VB can be visible as a broad feature, as previously observed for this material.[22] Nevertheless, the data taken using a photon energy of $h\nu$ = 18 eV actually shows a weak band reaching a binding energy of ≈300 meV between the branches of the topological surface state (see red arrow in Fig. 1(c)). We assign this to the bottom of the VB. The data taken at 22 eV also shows this band, or at least a continuum with an edge following the same dispersion (red arrow in Fig. 1(d)). Given the fact that the upper VB reaches its highest binding energy at these photon energies, it is possible to assign the spectra taken at $h\nu$ = 18 eV and $h\nu$ = 22 eV to a region around the Z point of the BZ. The detailed k_z dispersion of the features will be clarified below. The spectrum in Fig. 1(e) taken at 27 eV photon energy is entirely different. The topological surface state is much more pronounced and there is little photoemission intensity between the surface state branches. The qualitative similarity to data taken from Bi_2Se_3 (see online supplementary material of ref. 29) suggests that the data is taken near the Γ point of the BZ where the top of the VB should be visible. However, in Bi_2Se_3, the VBM at Γ is never actually observed because its dispersion almost coincides with the lower part of the topological surface state Dirac cone.

The highest VB in the $\bar{\Gamma}$–$\bar{M}$ plane is seen in Fig. 1(c) as a diffuse intensity at E_F and in Fig. 1(d) as a band moving up to E_F (marked by a green arrow). The band does not appear to cross E_F but rather levels off and shows a flat dispersion ≈30 meV below E_F. Finding this band at the photon energies corresponding to $k_z \approx Z$ for normal emission (rather than to $k_z \approx \Gamma$) is expected from its calculated position in the bulk BZ (see dispersion along Z–F in Fig. 1(b)).[10] When mapping the photoemission intensity at the Fermi level in two-dimensional $\mathbf{k}$ space, this band gives rise to six "flower petals" along $\bar{\Gamma}$–$\bar{M}$ (this can be seen in Fig. 2(a) in ref. 27 using data taken from the same crystal as here at $h\nu$ = 22 eV, and in ref. 6 and 25).

A more systematic investigation of the k_z-dependent bulk band structure in the $\bar{\Gamma}$–$\bar{M}$ plane is shown in Fig. 2. Here, k_z of the outgoing photoelectrons and thereby also the k_z-dependence of the initial states is explored by collecting photon energy-dependent data. The photon energies have been converted into k_z values using a free electron final state model. Assuming a work function of ≈5.0 eV[30] and an inner potential of V_0 = 12.8 eV reproduces the position of a Z point at $h\nu$ = 22 eV. The corresponding k_z value is 2.795 Å^{-1} which is 9 times the bulk Γ–Z distance. The same Z point is observed at a photon energy of ≈26.6 eV for Bi_2Se_3. For higher photon

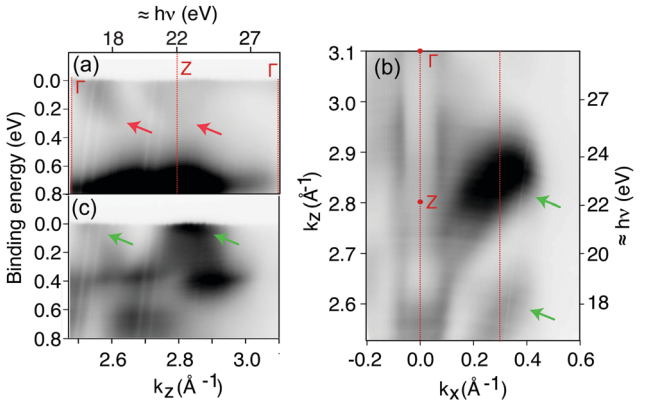

Fig. 2 (a) Photoemission intensity as a function of binding energy and k_z in normal emission. The spectrum is integrated along k_x within ±0.02 Å^{-1} around normal emission. (b) Photoemission intensity at the Fermi energy as a function of k_z and k_x. The spectrum is integrated within ± 100 meV around the Fermi level. The $h\nu$ scale is strictly correct for normal emission and the Fermi energy and otherwise only approximate. (c) Photoemission intensity as a function of binding energy and k_z for k_x = 0.3 Å^{-1}, integrated within ±0.02 Å^{-1} around this value. The colour scale is chosen such that some features are saturated.

energies, we find indications of Z points at $h\nu$ = 54.4 and 74.8 eV (not shown). These also agree with the free electron final state model.

Fig. 2(a) shows the photoemission intensity as a function of binding energy and k_z collected in normal emission. The data are similar to the corresponding observation for Bi_2Se_3 (see Fig. 6 in ref. 31). A broad parabolic feature is visible near E_F, reaching its highest binding energy at $k_z \approx$ 2.8 Å^{-1} (red arrow). We identify this as the bottom of the uppermost VB at Z. A similar structure is visible at lower k_z, reaching the highest binding energy at around 2.6 Å^{-1} (also marked by a red arrow). These observations are consistent with the position of the uppermost VB in Fig. 1(c) and (d) since the two k_z values correspond to photon energies of 18 and 22 eV, respectively. However, the free electron final state model cannot explain the observation of the upper VB minimum at $h\nu$ = 18 eV (≈2.6 Å^{-1}, as seen in Fig. 1(c) and 2(b)), as this k_z value does not correspond to a Z point. A similar feature for Bi_2Se_3 was assigned to a surface umklapp process.[31] The same explanation may hold here but the emission could also occur *via* the non-free electron like nature of the final states at the low photon energies used here.

Having identified the bulk Z point in the data, we move our attention to the VBM in the $\bar{\Gamma}$–$\bar{M}$ plane that is expected to be found at a similar k_z. To this end, Fig. 2(b) shows the photoemission intensity at the Fermi energy as a function of k_z and k_x along $\bar{\Gamma}$–$\bar{M}$. Pronounced features are the two vertical streaks that correspond to the Fermi level crossings of the topological surface state. In addition, two dispersive broad structures are visible around k_x = 0.3 Å^{-1} and at k_z values around 2.6 and 2.8 Å^{-1} (marked by green arrows). These stem from the VBM in the $\bar{\Gamma}$–$\bar{M}$ plane and are also seen in Fig. 1(c) and (d). The shape of the high intensity features agrees remarkably well with the calculated constant energy contours for the VB in Fig. 3 of ref.

Published on 12 November 2021. Downloaded on 1/20/2026 5:39:56 PM.

10. Fig. 2(c) shows the dispersion of these structures (also marked by green arrows) with k_z by plotting the photoemission intensity as a function of photon energy in the same way as in Fig. 2(a) but for k_x = 0.3 Å^{-1}. The presence of a dispersion with k_z is evident. As in the selected data of Fig. 1(d), it appears as if the band barely reaches the Fermi level without actually crossing it. This view is also supported by the lack of sharp structures in Fig. 2(b) such that the ''islands'' of high intensity can be interpreted as a spill-out of the intensity from band maxima below E_F, rather than distinct crossings.

In order to confirm this interpretation and to investigate the position of the VB along $\bar{\Gamma}$–$\bar{M}$ further, we gain access to the usually unoccupied band structure by adsorbing a low coverage of Rb atoms onto the surface while collecting ARPES data. This leads to doping with electrons and to a downward band bending at the surface.[32] We can track the occupation of the topological surface state and the normally unoccupied VB, and even populate the bottom of the conduction band. We perform the doping experiment at two photon energies, 22 eV and 18 eV to be close to the Z point expected for free electron final states at 22 eV and to the Z point-like features reached at 18 eV.

Fig. 3(a) shows the photoemission intensity at normal emission for $h\nu$ = 22 eV as a function of time while dosing Rb atoms onto the surface. The beginning and end of the Rb exposure are marked on the time axis. Fig. 3(b) gives the corresponding photoemission intensity at the Fermi energy and along k_x. Fig. 3(c)–(e) show snapshots of the electronic structure at selected times. Fig. 3(c) was acquired prior to starting the Rb deposition and is thus very similar to Fig. 1(d). The band forming the VBM along k_x is marked by a green arrow. Upon Rb dosing the observed bands shift to higher binding energy. After the end of the exposure, the features gradually move back to lower binding energy. This could either be due to Rb desorption or intercalation. Scanning the UV light spot across the sample shows that the shift takes place over the entire sample surface and is not induced by the UV radiation. The amount of Rb present on the sample surface after 60 s of deposition was estimated to be 0.1 monolayer, determined from the ratio between Rb and Te core level photoemission intensities.

As discussed above and seen in Fig. 3(a) and (c), the uppermost VB at normal emission appears to be a broad feature between E_F and a binding energy of ≈300 meV. However, when exposing the surface to Rb, the VB features sharpen up and the photoemission intensity is concentrated in a narrow window around the bottom of the band. This can be explained by a quantisation of the VB states due to a downward bending of the bands near the surface, as such a quantization removes the k_z broadening. Naively, a quantisation upon *downward* bending of the band is expected for the conduction band, not for the VB, but for this class of materials the VB width is so small that the bands become confined once the amount of band bending exceeds the width of the VB, as has been shown for Bi_2Se_3.[33] The VB quantisation turns the three-dimensional dispersion into two-dimensional sub-bands that no longer disperse in k_z. The precise location of the VBM at Γ therefore remains

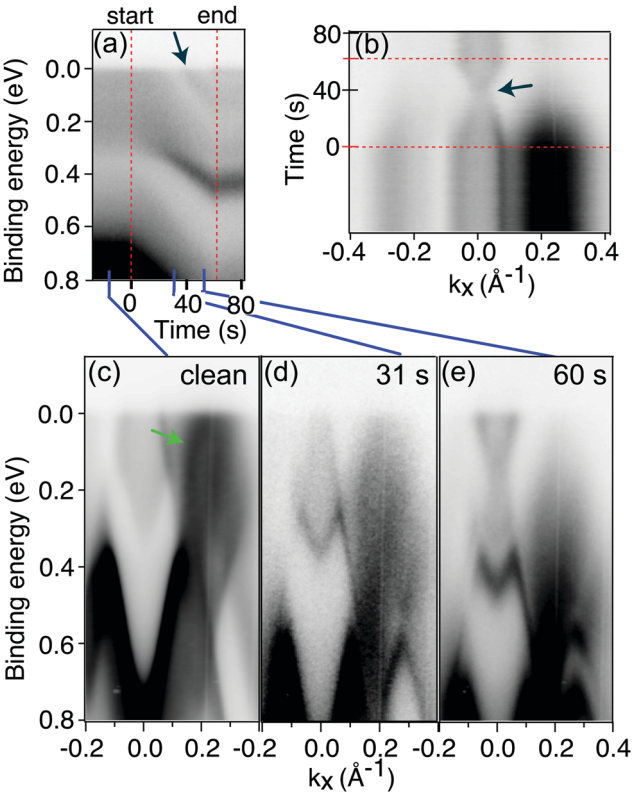

Fig. 3 Rb dosing at 22 eV. (a) Photoemission intensity in normal emission as a function of binding energy and time while dosing Rb atoms on the surface. Red dashed lines mark the start and end of the Rb dosing. The spectrum is integrated ±0.02 Å^{-1} around normal emission. The black arrow marks the time at which the Dirac point of the topological surface state crosses E_F. (b) Photoemission intensity at the Fermi level as a function of time and k_x while dosing Rb atoms onto the surface. The spectrum is integrated ±100 meV around the Fermi level. (c)–(e) Photoemission intensity as a function of binding energy and k_x acquired at different moments in time after beginning the Rb dosing. (c) Was obtained by integrating the data in (a) from the beginning up until the first red line and (e) was obtained by integrating from the last red marker up until the end of the acquisition. The colour scale of spectra (a) and (c)–(e) was chosen such that some features are saturated.

inaccessible. We tentatively place the VBM just below the Dirac point. This is consistent with previous observations[22] and also with the fact that a weak diffuse photoemission intensity remains inside the lower part of the surface state Dirac cone in Fig. 3(d) and (e).

After a Rb exposure time of 32 s, an additional band can be observed to cross E_F and move to high binding energies in Fig. 3(a) (black arrow). It originates from the Dirac point of the topological surface state. This can be clearly seen when inspecting the time dependence of the photoemission intensity at E_F shown in Fig. 3(b), where the lines representing the Fermi level crossings of the topological surface states start to converge upon Rb dosing and cross at the same time as the state in Fig. 3(a) becomes visible, bringing the Dirac cone from the hole-doped to the electron-doped regime. Note also that the intensity at E_F around $k \approx \pm 0.3$ Å^{-1} vanishes in Fig. 3(b) upon doping. As these features correspond to the VBM in the $\bar{\Gamma}$–$\bar{M}$ plane, such a shift

 This journal is © the Owner Societies 2021

Published on 12 November 2021. Downloaded on 1/20/2026 5:39:56 PM.

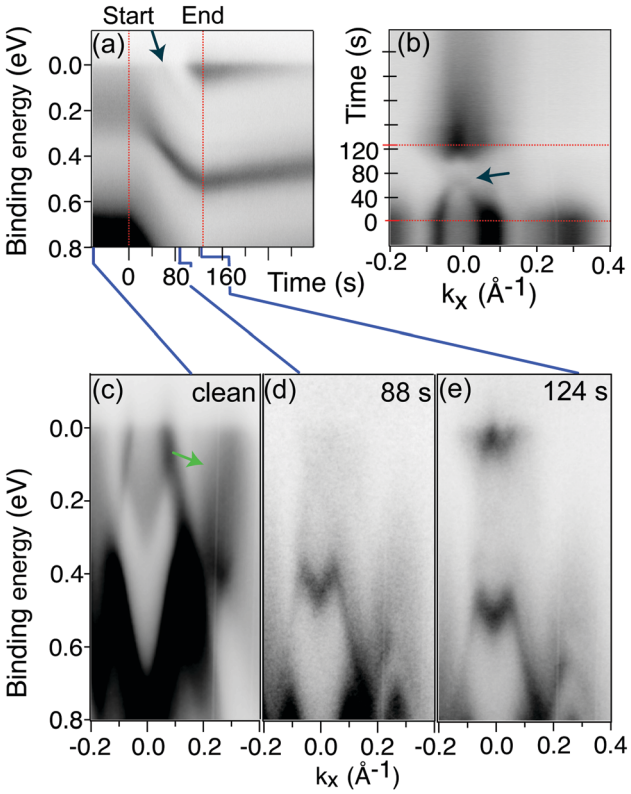

Fig. 4 Rb dosing at 18 eV. The panels correspond to those in Fig. 3. The data for panel (e) has been integrated over 3 s.

suggests that the VBM is at higher binding energy than the Dirac point. Inspecting energy- and k_x-dependent spectra at different Rb coverages (Fig. 3(c)–(e)) appears to confirm this.

A similar behaviour is observed in Fig. 4 where doping-dependent ARPES data acquired at $h\nu$ = 18 eV is shown. The data are presented in the same way as in Fig. 3 and the conclusions about the position of the VBM in the $\bar{\Gamma}$–$\bar{M}$ plane are largely the same. The band dispersion is less clear, even for the clean surface. Nevertheless, the photoemission intensity from the VBM along $\bar{\Gamma}$–$\bar{M}$ seen in Fig. 3(b) quickly vanishes in Fig. 4(b) and the band maximum can be clearly placed below the surface state Dirac point. An important difference to Fig. 3 is that the Rb exposure was carried out for a longer time (120 s, giving rise to a coverage of 0.3 monolayers). As seen in Fig. 3(e), this leads to an occupation of the conduction band (possibly present as a quantized state). Note that the observation of conduction band states does not permit the determination of the bulk band gap, as the conduction band minimum is not found at Z but close to Γ.[10] Furthermore, alkali-induced surface doping does not necessarily conserve the gap size as seen by comparing ref. 34 and 35, for instance.

Combining the data for the clean and Rb-covered surface, we can conclude the following about the VB in the $\bar{\Gamma}$–$\bar{M}$ plane: The plane does indeed contain a local VBM. However, its energy is lower than that of the global VBM at the Γ point, which we assume to be just below the Dirac point of the surface state. The dispersion of the upper VB in $\bar{\Gamma}$–$\bar{M}$ shows a maximum 30 meV below E_F for data taken at $h\nu$ = 22 eV (see Fig. 1(d) and 3(c)). This feature broadens out upon Rb dosing but we do not find any indication of a higher lying maximum. When determining the position of the surface state Dirac point by extrapolation of the linear dispersion above E_F for the clean surface, we find the $\bar{\Gamma}$–$\bar{M}$ VBM to be 170 meV ± 43 meV below the surface state Dirac point. These findings clearly support the dispersion obtained by GW calculations.[10] We can rule out the DFT results which place the $\bar{\Gamma}$–$\bar{M}$ VBM above the surface state Dirac point.[2,11]

With this relation between surface and bulk electronic structure, Sb_2Te_3 is a potential material for realising surface state-dominated transport near the Dirac point upon suitable doping. This is a remarkable property for a binary TI compound that – due to the energetic vicinity of surface Dirac point and bulk valence bands – is absent in Bi_2Se_2[19] and Bi_2Te_2.[20] While all these materials are plagued by different kinds of degenerate bulk doping, this issue can be resolved for Bi_2Te_2Se such as to achieve surface state-dominated transport.[21,36] Realizing an insulating bulk and a surface state Fermi level very close to the Dirac point requires the synthesis of even more complex alloys.[37]

4 Conclusions

In conclusion, we have determined the band structure of the topmost VB of Sb_2Te_3 by synchrotron radiation-based ARPES, with the objective to find the position of the global VBM. We find a predicted VBM in the BZ plane given by the $\bar{\Gamma}$–$\bar{M}$ azimuthal direction. The binding energy of this band is below the surface state Dirac point. This is significantly different from predictions by DFT but in line with calculations employing GW corrections. The high binding energy of the local VBM implies that it should be possible to achieve surface state dominated electronic transport near the Dirac point for Sb_2Te_3.

Conflicts of interest

There are no conflicts to declare.

Acknowledgements

This work was supported by VILLUM FONDEN *via* the Centre of Excellence for Dirac Materials (grant no. 11744) and the Young Investigator Program (grant no. 15375). We thank Anton Tamtögl for fruitful discussions.

Notes and references

1 H. Zhang, C.-X. Liu, X.-L. Qi, X. Dai, Z. Fang and S.-C. Zhang, *Nat. Phys.*, 2009, **5**, 438–442.
2 D. Hsieh, Y. Xia, D. Qian, L. Wray, F. Meier, J. H. Dil, J. Osterwalder, L. Patthey, A. V. Fedorov, H. Lin, A. Bansil, D. Grauer, Y. S. Hor, R. J. Cava and M. Z. Hasan, *Phys. Rev. Lett.*, 2009, **103**, 146401.

Published on 12 November 2021. Downloaded on 1/20/2026 5:39:56 PM.

3 Y. Ando, *J. Phys. Soc. Jpn.*, 2013, **82**, 102001.
4 J. Horák, Z. Starý and J. Klikorka, *Phys. Status Solidi B*, 1988, **147**, 501–510.
5 M. Z. Hasan and C. L. Kane, *Rev. Mod. Phys.*, 2010, **82**, 3045–3067.
6 C. Seibel, H. Maaß, M. Ohtaka, S. Fiedler, C. Jünger, C.-H. Min, H. Bentmann, K. Sakamoto and F. Reinert, *Phys. Rev. B: Condens. Matter Mater. Phys.*, 2012, **86**, 161105.
7 J. Reimann, J. Güdde, K. Kuroda, E. V. Chulkov and U. Höfer, *Phys. Rev. B: Condens. Matter Mater. Phys.*, 2014, **90**, 081106.
8 Y. Jiang, Y. Wang, M. Chen, Z. Li, C. Song, K. He, L. Wang, X. Chen, X. Ma and Q.-K. Xue, *Phys. Rev. Lett.*, 2012, **108**, 016401.
9 L. Fu, C. L. Kane and E. J. Mele, *Phys. Rev. Lett.*, 2007, **98**, 106803.
10 I. A. Nechaev, I. Aguilera, V. De Renzi, A. di Bona, A. Lodi Rizzini, A. M. Mio, G. Nicotra, A. Politano, S. Scalese, Z. S. Aliev, M. B. Babanly, C. Friedrich, S. Blügel and E. V. Chulkov, *Phys. Rev. B: Condens. Matter Mater. Phys.*, 2015, **91**, 245123.
11 T. V. Menshchikova, S. V. Eremeev and E. V. Chulkov, *JETP Lett.*, 2011, **94**, 106.
12 E. Kioupakis, M. L. Tiago and S. G. Louie, *Phys. Rev. B: Condens. Matter Mater. Phys.*, 2010, **82**, 245203.
13 O. V. Yazyev, E. Kioupakis, J. E. Moore and S. G. Louie, *Phys. Rev. B: Condens. Matter Mater. Phys.*, 2012, **85**, 161101.
14 I. A. Nechaev and E. V. Chulkov, *Phys. Rev. B: Condens. Matter Mater. Phys.*, 2013, **88**, 165135.
15 I. Aguilera, C. Friedrich, G. Bihlmayer and S. Blügel, *Phys. Rev. B: Condens. Matter Mater. Phys.*, 2013, **88**, 045206.
16 T. Förster, P. Krüger and M. Rohlfing, *Phys. Rev. B*, 2016, **93**, 205442.
17 J. Vidal, X. Zhang, L. Yu, J.-W. Luo and A. Zunger, *Phys. Rev. B: Condens. Matter Mater. Phys.*, 2011, **84**, 041109.
18 W. Zhang, R. Yu, H.-J. Zhang, X. Dai and Z. Fang, *New J. Phys.*, 2010, **12**, 065013.
19 I. A. Nechaev, R. C. Hatch, M. Bianchi, D. Guan, C. Friedrich, I. Aguilera, J. L. Mi, B. B. Iversen, S. Blügel, P. Hofmann and E. V. Chulkov, *Phys. Rev. B: Condens. Matter Mater. Phys.*, 2013, **87**, 121111.
20 M. Michiardi, I. Aguilera, M. Bianchi, V. E. de Carvalho, L. O. Ladeira, N. G. Teixeira, E. A. Soares, C. Friedrich, S. Blügel and P. Hofmann, *Phys. Rev. B: Condens. Matter Mater. Phys.*, 2014, **90**, 075105.
21 L. Barreto, L. Kühnemund, F. Edler, C. Tegenkamp, J. Mi, M. Bremholm, B. B. Iversen, C. Frydendahl, M. Bianchi and P. Hofmann, *Nano Lett.*, 2014, **14**, 3755–3760.
22 C. Pauly, G. Bihlmayer, M. Liebmann, M. Grob, A. Georgi, D. Subramaniam, M. R. Scholz, J. Sánchez-Barriga, A. Varykhalov, S. Blügel, O. Rader and M. Morgenstern, *Phys. Rev. B: Condens. Matter Mater. Phys.*, 2012, **86**, 235106.
23 C. Seibel, H. Maaß, H. Bentmann, J. Braun, K. Sakamoto, M. Arita, K. Shimada, J. Minár, H. Ebert and F. Reinert, *J. Electron Spectrosc. Relat. Phenom.*, 2015, **201**, 110–114.
24 G. Wang, X. Zhu, J. Wen, X. Chen, K. He, L. Wang, X. Ma, Y. Liu, X. Dai, Z. Fang, J. Jia and Q. Xue, *Nano Res.*, 2010, **3**, 874.
25 L. Plucinski, A. Herdt, S. Fahrendorf, G. Bihlmayer, G. Mussler, S. Döring, J. Kampmeier, F. Matthes, D. E. Bürgler, D. Grützmacher, S. Blügel and C. M. Schneider, *J. Appl. Phys.*, 2013, **113**, 053706.
26 Y. Jiang, Y. Y. Sun, M. Chen, Y. Wang, Z. Li, C. Song, K. He, L. Wang, X. Chen, Q.-K. Xue, X. Ma and S. B. Zhang, *Phys. Rev. Lett.*, 2012, **108**, 066809.
27 A. Ruckhofer, S. Halbritter, H. E. Lund, A. J. U. Holt, M. Bianchi, M. Bremholm, G. Benedek, P. Hofmann, W. E. Ernst and A. Tamtögl, *Phys. Chem. Chem. Phys.*, 2021, **23**, 7806–7813.
28 S. V. Hoffmann, C. Søndergaard, C. Schultz, Z. Li and P. Hofmann, *Nucl. Instrum. Methods Phys. Res., Sect. A*, 2004, **523**, 441.
29 M. Bianchi, D. Guan, S. Bao, J. Mi, B. B. Iversen, P. D. C. King and P. Hofmann, *Nat. Commun.*, 2010, **1**, 128.
30 G. Hao, X. Qi, G. Wang, X. Peng, S. Chang, X. Wei and J. Zhong, *RSC Adv.*, 2012, **2**, 10694.
31 M. Bianchi, R. C. Hatch, D. Guan, T. Planke, J. Mi, B. B. Iversen and P. Hofmann, *Semicond. Sci. Technol.*, 2012, **27**, 124001.
32 M. Bianchi, R. C. Hatch, Z. Li, P. Hofmann, F. Song, J. Mi, B. B. Iversen, Z. M. Abd El-Fattah, P. Löptien, L. Zhou, A. A. Khajetoorians, J. Wiebe, R. Wiesendanger and J. W. Wells, *ACS Nano*, 2012, **6**, 7009–7015.
33 M. Bianchi, R. C. Hatch, J. Mi, B. B. Iversen and P. Hofmann, *Phys. Rev. Lett.*, 2011, **107**, 086802.
34 J. A. Miwa, S. Ulstrup, S. G. Sørensen, M. Dendzik, A. G. Čabo, M. Bianchi, J. V. Lauritsen and P. Hofmann, *Phys. Rev. Lett.*, 2015, **114**, 046802.
35 A. Grubišić Čabo, J. A. Miwa, S. S. Grønborg, J. M. Riley, J. C. Johannsen, C. Cacho, O. Alexander, R. T. Chapman, E. Springate, M. Grioni, J. V. Lauritsen, P. D. C. King, P. Hofmann and S. Ulstrup, *Nano Lett.*, 2015, **15**, 5883.
36 Z. Ren, A. A. Taskin, S. Sasaki, K. Segawa and Y. Ando, *Phys. Rev. B: Condens. Matter Mater. Phys.*, 2010, **82**, 241306.
37 T. Arakane, T. Sato, S. Souma, K. Kosaka, K. Nakayama, M. Komatsu, T. Takahashi, Z. Ren, K. Segawa and Y. Ando, *Nat. Commun.*, 2012, **3**, 636.

 This journal is © the Owner Societies 2021